




Ideal hourglass-type charge-three Weyl fermions in spinless systems

Xiaoliang Xiao ¹, Yuanjun Jin ², Da-Shuai Ma,^{1,3} Weixiang Kong,¹ Jing Fan ⁴, Rui Wang,^{1,3,5} and Xiaozhi Wu^{1,5,*}

¹*Institute for Structure and Function & Department of Physics, Chongqing University, Chongqing 400044, People's Republic of China*

²*Division of Physics and Applied Physics, School of Physical and Mathematical Sciences,*

Nanyang Technological University, Singapore 637371, Singapore

³*Center of Quantum Materials and Devices, Chongqing University, Chongqing 400044, People's Republic of China*

⁴*Center for Computational Science and Engineering, Southern University of Science and Technology, Shenzhen 518055, People's Republic of China*

⁵*Chongqing Key Laboratory for Strongly Coupled Physics, Chongqing 400044, People's Republic of China*



(Received 15 August 2023; revised 11 October 2023; accepted 7 February 2024; published 26 February 2024)

Hourglass-type Weyl fermions with the maximally topological charge of $|C| = 3$, namely hourglass-type charge-three Weyl fermions (CTWFs), have seldom been reported due to the nonnegligible spin-orbit coupling effect and Pauli exclusion principles. Here, based on symmetry arguments and the low-energy effective $\mathbf{k} \cdot \mathbf{p}$ model, we confirm that two chiral space groups (SGs), i.e., SG $P6_3$ (No. 173) and SG $P6_322$ (No. 182), can host ideal hourglass-type CTWFs in spinless systems. Moreover, we take Li_2CO_4 as a concrete example to show the ideal hourglass-type CTWFs, which possess ultralong sextuple- and triple-helicoid Fermi arcs, making them easier to be detected by experiments. Our work not only offers an avenue to search for ideal hourglass-type CTWFs but also provides a promising platform for experiments to verify this kind of unconventional quasiparticles with the ultralong sextuple- and triple-helicoid surface arcs.

DOI: [10.1103/PhysRevB.109.075160](https://doi.org/10.1103/PhysRevB.109.075160)

I. INTRODUCTION

Hourglass-type Weyl fermions (WFs) have been theoretically proposed for many years [1–3]. This new class of WFs was originally predicted on the (010) surface of nonsymmorphic crystal materials KHgX ($X = \text{As}, \text{Sb}, \text{Bi}$) [1] and then observed in experiments via angle-resolved photoemission spectroscopy [4,5]. Subsequently, it was extended to a series of nonmagnetic (magnetic) space groups (SGs) by the compatibility relations [6,7] and widely found in the electronic structures of nonsymmorphic material, including three-dimensional (3D) ReO_2 [8], Ag_2BiO_3 [9,10], AgF_2 [11], and Mg_2VO_4 [12], as well as two-dimensional (2D) $\text{Bi/ClSiC}(111)$ [13] and GaTeI [14]. Furthermore, various hourglass-type fermions have been proposed successively, such as hourglass-type Weyl/Dirac points [6,13,15–17], hourglass-type Weyl/Dirac loops [11,14,17], hourglass-type Weyl/Dirac chains [8,18], and beyond [10,12].

Among these hourglass-type WFs mentioned above, one of the most important members is hourglass-type charge-three WFs (CTWFs), which possess the maximally topological charge of $|C| = 3$ [19]. This hourglass-type crossing owns the nonlinear dispersion in the plane and the linear dispersion out of the plane [see Figs. 1(a) and 1(b)], leading to fancy physical properties, such as multiple and longer Fermi arcs [20–26], larger quantized circular photogalvanic effect (CPGE) [27–29], non-Fermi-liquid interaction effects [30,31], and quantum criticality and phase transition [32,33], etc.

Recently, in bosonic systems, the hourglass-type charge-three Weyl phonons have been revealed [34,35]. However, unlike bosons, the fermion-type quasiparticles are restrained by the Pauli exclusion principles, and the well-known spin-orbit coupling (SOC) mechanism would break or shift the band crossings of hourglass-type CTWFs. For example, due to the SOC effect, the intercalated transition metal dichalcogenides form two hourglass-type WFs above and below the Fermi level [36], whose topological surface states (TSSs) entangle with the bulk states and depend on the strength of SOC. Therefore, it is necessary to realize ideal hourglass-type CTWFs in spinless systems.

Fortunately, there are indeed two cases that can be considered as the ideal platforms for realizing hourglass-type CTWFs in spinless systems. One case is a fully spin-polarized magnetic system, in which hourglass CTWFs can occur in a spin channel with 100% spin polarization. It has been proposed in crystal materials $P6_322$ -type XNiIO_6 ($X = \text{Ba}, \text{Sr}$) [37,38]. However, in such magnetic systems, it is not easy to determine magnetic ground states and Hubbard-Coulomb interaction U -values. Besides, such systems usually also involve heavy atoms with strong SOC, which would break hourglass-type CTWFs. Another case is nonmagnetic systems with negligible SOC. There are different kinds of light-atom-composed crystals to achieve various topological states [39–54] because $\text{SU}(2)$ symmetry is conserved [55]. Thus, these ultralightweight materials are promising platforms to realize ideal hourglass-type CTWFs.

Here, based on symmetry arguments and the low-energy effective model, we identify two chiral SGs (No. 173 and No. 182) that can possess ideal hourglass-type CTWFs in

*xiaozhiwu@cqu.edu.cn

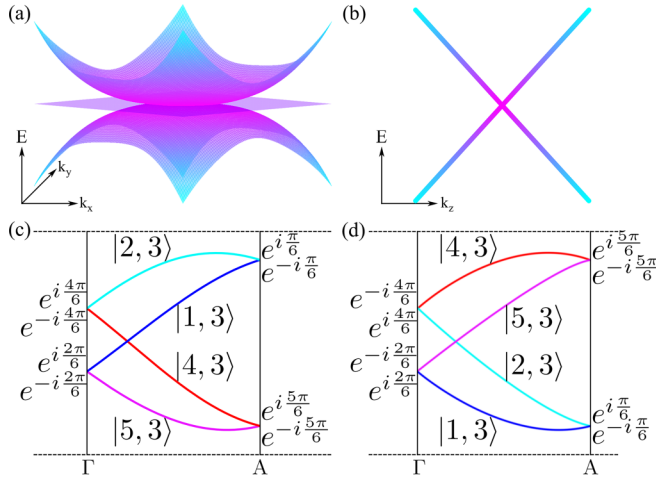


FIG. 1. (a) and (b) The band dispersions of the neck crossing of the hourglass-type CTWF in the plane and out of the plane, which show the nonlinear and linear dispersions. (c) and (d) Two modes of the hourglass-type CTWF along the Γ -A path. The Γ and A points possess two natural 2D IRs.

spinless systems. As two CTWFs connected by time-reversal symmetry (\mathcal{T}) occur along the Γ -A direction, it can generate unique sextuple- and triple-helicoid Fermi arcs on the (001) and (10 $\bar{1}$ 0) surface Brillouin zones (BZs). Furthermore, by the first-principles calculations, we take the crystal material Li_2CO_4 with SG $P6_3$ (No. 173) as an example to confirm the existence of ideal hourglass-type CTWFs. The calculated results show that the ultralong sextuple- and triple-helicoid Fermi arcs do appear on the (001) and (10 $\bar{1}$ 0) surface BZs. Our work not only offers an avenue to achieve ideal hourglass-type CTWFs but also provides a great platform for exploring unique chirality-dependent physical properties associated with unconventional quasiparticles.

II. COMPUTATIONAL METHODS

We carry out first-principles calculations within the framework of density functional theory (DFT) [56,57] using the Vienna *ab initio* simulation package (VASP) [58,59]. The exchange-correlation interactions are described by the generalized gradient approximation (GGA) with the Perdew-Burke-Ernzerhof (PBE) functional [60]. We treat the electron-ion interactions by the projector-augmented-wave (PAW) potentials [61]. The kinetic energy cutoff of the plane wave is set to be 550 eV. The first BZ is sampled at a Γ -centered \mathbf{k} mesh with $8 \times 8 \times 5$ and $13 \times 13 \times 8$ for structural optimizations and the self-consistent of total energy, respectively [62]. All geometric structures fully relax until energy and force converge to 10^{-6} eV and 0.01 eV/Å. The phonon spectra are calculated to examine the dynamic stability by using PHONOPY code [63] through the density functional perturbation theory (DFPT) approach [64].

III. SYMMETRY ARGUMENTS AND THE LOW-ENERGY EFFECTIVE MODEL

First, we perform symmetry arguments to search for all candidate SGs that allow the existence of ideal

hourglass-type CTWFs in spinless systems. For fermionic systems with \mathcal{T} symmetry, as shown in previous works [19,65–67], the CTWFs can occur on the sixfold rotational axis of chiral SGs (No. 168 ~ 173 and No. 177 ~ 182). Therefore, it only appears on the C_6 -invariant high symmetry point (HSP) or line (HSL), in which two bands host different eigenvalues of the sixfold (screw) rotational operator. The sixfold (screw) rotational symmetry is represented as $\tilde{C}_{6z,m}^n = \{C_{6z}^n | 00\frac{m}{6}\}$ ($n = 0, 1, \dots, 5$; $m = 0, 1, \dots, 5$) along the Γ -A direction, whose eigenvalues can be expressed as $e^{i2\pi\frac{n}{6}} e^{-ik_z\frac{m}{6}}$, marked as $E_{n,m}$, and the corresponding Bloch states can be chosen as eigenstates of $\tilde{C}_{6z,m}^n$, namely $|n, m\rangle$. These eigenvalues and eigenstates are listed in Table I. Hence, two bands with $|n_1, m\rangle$ and $|n_2, m\rangle$, where $n_1 \neq n_2$, can form three types of WFs, e.g., $|C| = 1$, $|C| = 2$, and $|C| = 3$ WFs [65]. However, the CTWFs can only be formed by the two bands with $|n, m\rangle$ and $|n + 3 \bmod 6, m\rangle$, of which the ratio of eigenvalues is -1 , i.e., $E_{n_1,m}/E_{n_2,m} = -1$ [67]. To form the hourglass-type CTWFs, the Γ and A points must host two doubly degenerate states, and two of them are switched between the Γ and A points; see the dispersion feature in Figs. 1(c) and 1(d). Let's start with the degenerate states of the Γ point. Under sixfold rotational symmetry, there are two different 2D irreducible representations (IRs) due to \mathcal{T} symmetry with the product of $\mathcal{T}^2 = 1$ [15,68,69]. Here, the complex conjugated states are doubly degenerate, i.e., $|e^{i\frac{4\pi}{6}}, e^{-i\frac{4\pi}{6}}\rangle$ and $|e^{i\frac{2\pi}{6}}, e^{-i\frac{2\pi}{6}}\rangle$; see the Γ point in Fig. 1(c). Owing to half lattice translation, all of the doubly degenerate states pick up the phase of $\pm i$ and evolve into other two paired complex conjugated states at the A point. The two doubly degenerated states become $|e^{i\frac{\pi}{6}}, e^{-i\frac{\pi}{6}}\rangle$ and $|e^{i\frac{5\pi}{6}}, e^{-i\frac{5\pi}{6}}\rangle$; see the A point in Fig. 1(c). All the eigenvalues are summarized in Tables I and SI in the Supplemental Material (SM) [70]. Since complex conjugated states evolve into new different degenerated states, it simultaneously forms an intrinsic crossing point between Γ and A. This produces the symmetry-enforced crossing points, so-called hourglass-type WFs [Figs. 1(c) and 1(d)]. Besides, the two bands near the neck crossing are the states, either $|1, 3\rangle$ and $|4, 3\rangle$ [see Fig. 1(c)] or $|2, 3\rangle$ and $|5, 3\rangle$ [see Fig. 1(d)], indicating that the neck crossing here must be an hourglass-type CTWF. Thus, it implies that only two chiral SGs (No. 173 and No. 182) meet our criterion.

Now, we further construct the two-band low-energy effective $\mathbf{k} \cdot \mathbf{p}$ model near the neck crossing to prove such hourglass-type WF with the topological charge of $|C| = 3$. It usually possesses the following form:

$$\mathcal{H}(\mathbf{k}) = h(\mathbf{k})\sigma_+ + h^*(\mathbf{k})\sigma_- + g(\mathbf{k})\sigma_z, \quad (1)$$

where $\sigma_{\pm} = (\sigma_x \pm i\sigma_y)/2$, $\sigma_{x(y,z)}$ are three Pauli matrices, and $h(\mathbf{k})$ and $g(\mathbf{k})$ represent the complex and real functions, respectively. According to our above analysis, the two states $|1, 3\rangle$ and $|4, 3\rangle$ between Γ and A are symmetry enforced to form the CTWF in hourglass-type CTWF systems; we thus select them as the basis of two-band Hamiltonian [see Fig. 1(c)]. The eigenvalues are $e^{i\pi/3} e^{-ik_z/2}$ and $e^{i4\pi/3} e^{-ik_z/2}$, denoted by $E_{1,3}$ and $E_{4,3}$. Hence, matrix representation of $\tilde{C}_{6z,3}^1$ is given by

$$D(\tilde{C}_{6z,3}^1) = \begin{bmatrix} E_{1,3} & 0 \\ 0 & E_{4,3} \end{bmatrix}. \quad (2)$$

TABLE I. The generators of SGs (No. 168~173 and No. 177 ~ 182), the high symmetry point (HSP) or line (HSL), eigenstates $|n, m\rangle$, and eigenvalues $e^{i2\pi\frac{n}{6}}e^{-ik_z\frac{m}{6}}$ ($n = 0, 1, \dots, 5; m = 0, 1, \dots, 5$).

Generators	HSP(or HSL)	$ 0, m\rangle$	$ 1, m\rangle$	$ 2, m\rangle$	$ 3, m\rangle$	$ 4, m\rangle$	$ 5, m\rangle$
$\{C_{6z} 00\frac{m}{6}\}, \mathcal{T}$	Γ	$e^{i2\pi\frac{0}{6}}$	$e^{i2\pi\frac{1}{6}}$	$e^{i2\pi\frac{2}{6}}$	$e^{i2\pi\frac{3}{6}}$	$e^{i2\pi\frac{4}{6}}$	$e^{i2\pi\frac{5}{6}}$
$\{C_{6z} 00\frac{m}{6}\}$	Γ -A	$e^{i2\pi\frac{0}{6}}e^{-ik_z\frac{m}{6}}$	$e^{i2\pi\frac{1}{6}}e^{-ik_z\frac{m}{6}}$	$e^{i2\pi\frac{2}{6}}e^{-ik_z\frac{m}{6}}$	$e^{i2\pi\frac{3}{6}}e^{-ik_z\frac{m}{6}}$	$e^{i2\pi\frac{4}{6}}e^{-ik_z\frac{m}{6}}$	$e^{i2\pi\frac{5}{6}}e^{-ik_z\frac{m}{6}}$
$\{C_{6z} 00\frac{m}{6}\}, \mathcal{T}$	A	$e^{i2\pi\frac{0}{6}}e^{-i\pi\frac{m}{6}}$	$e^{i2\pi\frac{1}{6}}e^{-i\pi\frac{m}{6}}$	$e^{i2\pi\frac{2}{6}}e^{-i\pi\frac{m}{6}}$	$e^{i2\pi\frac{3}{6}}e^{-i\pi\frac{m}{6}}$	$e^{i2\pi\frac{4}{6}}e^{-i\pi\frac{m}{6}}$	$e^{i2\pi\frac{5}{6}}e^{-i\pi\frac{m}{6}}$

The effective Hamiltonian under the constraint of the $\tilde{C}_{6z,3}$ -invariant symmetry is expressed as

$$D(\tilde{C}_{6z,3})\mathcal{H}(\mathbf{k})D^{-1}(\tilde{C}_{6z,3}) = \mathcal{H}(\tilde{C}_{6z,3}\mathbf{k}). \quad (3)$$

Thus, the Hamiltonian around the neck crossing expanded up to leading order reads

$$\begin{aligned} \mathcal{H}(\mathbf{k}) = & [(\alpha_1 k_+^3 + \alpha_2 k_-^3)\sigma_+ + \text{H.c.}] \\ & + [b_1 k_+ k_- + b_2 k_z]\sigma_z, \end{aligned} \quad (4)$$

where $\alpha_{1(2)}$ and $b_{1(2)}$ denote complex and real parameters depending on realistic materials, and $k_{\pm} = k_x \pm ik_y$. In this Hamiltonian, the band splittings are nonlinear in the k_x - k_y plane and linear out of this plane, as shown in Fig. S1 in the SM [70]. The unique nonlinear dispersions may lead to striking non-Fermi-liquid behaviors [71,72]. However, the topological charge is only decided by the leading order in the k_x - k_y plane, indicating the presence of a $|C| = 3$ WF. Then, we employ the Wilson-loop method to calculate the Wannier charge centers (WCCs) of this effective model [73], which shows that it is exactly an hourglass-type CTWF with $C = \pm 3$ (see Fig. S1 in the SM [70]). The results are also suitable for $|2, 3\rangle$ and $|5, 3\rangle$ eigenstates, as shown in Fig. 1(d).

IV. MATERIAL REALIZATION WITH ABUNDANT REAL CANDIDATES

Symmetry arguments and the low-energy effective model based on Eqs. (1)–(4) present a fundamental theoretical strategy to search for ideal hourglass-type CTWFs in two chiral SGs (No. 173 and No. 182). Then, high-throughput calculations are performed to search for the new materials, in which SGs are fixed to two chiral SGs (No. 173 and No. 182) and the occupied electrons are fixed to $4N + 2$. Herein, we only take a realistic crystal material Li_2CO_4 as an example to identify the existence of hourglass-type CTWFs. More material candidates are included in the SM [70]. As illustrated in Figs. 2(a) and 2(b), the crystal structure possesses 14 atoms in a unit cell, which crystallizes in SG $P6_3$ (No. 173). The Li, C, and O atoms are denoted by blue, black, and red balls, respectively. The Li atom locates at 2a (0, 0, 0.363) and 2b (0.333, 0.667, 0.305) Wyckoff positions, respectively. The C atom is at 2b (0.333, 0.667, 0.242) Wyckoff position. The O atom is located at 2b (0.333, 0.667, 0.059) and 6c (0.319, 0.396, 0.292) Wyckoff positions, respectively. The optimized lattice parameters satisfy $|\mathbf{a}| = |\mathbf{b}| = 5.01 \text{ \AA}$ and $|\mathbf{c}| = 7.54 \text{ \AA}$. Here, we also provide evidence of energetical, mechanical, and dynamical stability in the SM [70].

In Fig. 2(c), we show the bulk BZ and projected on the (001) and (10 $\bar{1}$ 0) surface BZs, in which the associated HSPs

are also marked. The SOC effect in Li_2CO_4 is negligible (see Fig. S1 in the SM [70]), which can be treated as an ideal spinless system. The bulk band structure along high-symmetry paths is shown in Fig. 3(a), which is pretty clean. There are three nonequivalent Weyl points (WPs), namely WF_1 , WF_2 , and WF_3 . By carefully scanning energy differences between the lowest conduction and the highest valence bands, we find that there are eight WPs over the whole BZ, including two hourglass-type CTWFs (WF_1) along the Γ -A path, related by \mathcal{T} symmetry, two WPs (WF_2) located at K, and other four WPs (WF_3) along the K-H direction [see Fig. 2(c)]. The detailed information is shown in Table II, including the corresponding energies, positions, topological charges, and multiplicities.

In this work, we mainly focus on hourglass-type CTWFs. Thus, we only plot the corresponding 3D representation in the k_x - k_y plane [see the inset of Fig. 3(a)] and the enlarged drawing of the energy dispersion along the Γ -A path [Fig. 3(b)]. It indicates that this CTWF possesses the nonlinear dispersion in the plane and the linear dispersion out of the plane, which is consistent with our model. Then, we also mark the IRs of point group (PG) C_6 . The related symbols of IRs are listed in Table SII in the SM [70,74]. One can find that there exist one-to-one

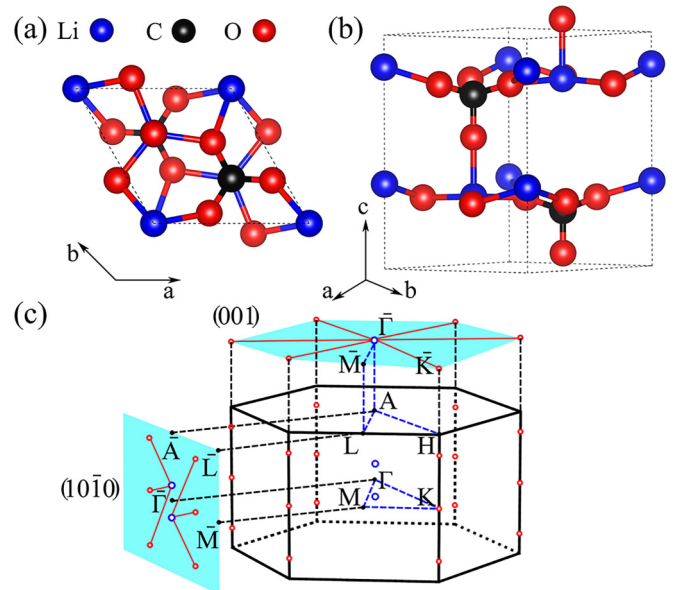


FIG. 2. (a) Top and (b) Side views of the crystal material Li_2CO_4 . (c) The bulk BZ and projected on the (001) and (10 $\bar{1}$ 0) surface BZs. The red lines of the (001) and (10 $\bar{1}$ 0) surface BZs represent the probable Fermi arcs. The marked circles in blue and red are the WPs with topological charges of -3 and $+1$, respectively.

TABLE II. The corresponding energies, positions, topological charges, and multiplicities of the inequivalent WPs in Li_2CO_4 .

Material	WP	$E-E_F$ (meV)	Coordinate (k_1, k_2, k_3)	Charge	Multiplicity
Li_2CO_4	WF_1	7.2	$(0, 0, \pm 0.116)$	-3	2
	WF_2	9.1	$\pm(0.333, 0.333, 0)$	+1	2
	WF_3	18.5	$\pm(0.333, 0.333, \pm 0.359)$	+1	4

corresponding relations in Tables I and SII, i.e., $\Gamma_2 \rightarrow |1, 3\rangle$, $\Gamma_3 \rightarrow |5, 3\rangle$, $\Gamma_5 \rightarrow |4, 3\rangle$, and $\Gamma_6 \rightarrow |2, 3\rangle$, for the sixfold screw rotational operation $C_{6,001}^+$. Hence, the Hamiltonian of this hourglass-type CTWF should satisfy Eq. (4), which leads to the topological charge of $C = -3$, as displayed in Fig. S1 in the SM [70]. Besides, it is worth noting that some materials may occur in another case, as shown in Fig. 3(c).

Then, we further examine the topological charges of each type of WPs in Li_2CO_4 by the first-principles calculations. To proceed with this, we constructed a tight-binding (TB) Hamiltonian by projecting the Bloch states into maximally localized Wannier functions using the WANNIER90 package [75,76]. As illustrated in Fig. 4(a), the calculated evolution of WCCs also shows that the WF_1 possesses a topological charge of $C = -3$, confirming an hourglass-type CTWF. This is consistent with the effective model. In Figs. 4(b) and 4(c), it exhibits that the WF_2 and WF_3 have a topological charge of $C = +1$. The sum of the topological charges in the whole BZ obeys the no-go theorem [77,78]. The Berry curvature distributions of the (001) and $(10\bar{1}0)$ surface BZs show that the WF_2 and WF_3 as the ‘‘source’’ flow into the ‘‘sink’’ generated by the WF_1 [Figs. 4(d) and 4(e)], which is consistent with the associated topological charges. As drawn in Fig. 2(c), the marked dots in red and blue in the BZ are the WPs with positive and negative topological charges, respectively. The red lines of the (001) and $(10\bar{1}0)$ surface BZs represent the probable Fermi arcs, which indicates the hourglass-type CTWFs should possess the unique nontrivial sextuple- and triple-helicoid surface arcs [Fig. 2(c)]. To prove this, we further calculate the local density of states (LDOSs) and Fermi arcs by employing the iterative Green’s function method with the WANNIERTOOLS package [79–81]. The LDOSs of the semi-infinite (001) and $(10\bar{1}0)$ surface BZs are shown in Figs. 5(a) and 5(e). Three branches of the visible TSSs start at the projection of CTWFs (WF_1) and terminate at the other WPs (WF_2

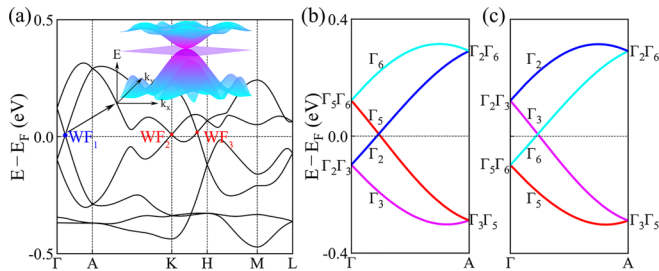


FIG. 3. (a) The bulk band structure of crystal material Li_2CO_4 along high-symmetry paths. The band crossings near the Fermi level are marked by WF_1 , WF_2 , and WF_3 , respectively. The inset is a 3D representation. (b) The enlarged drawings of energy dispersion along the Γ -A path and relevant IRs with PG C_6 . (c) Another possible mode of energy dispersion along the Γ -A path.

and WF_3). Additionally, it does occur cubic dispersion in the k_x - k_y plane. This is also consistent with the effective model. To clearly show their connections, the two isoenergy contours ($E_{\text{cut}_1} = 0$ meV and $E_{\text{cut}_2} = -3$ meV) are projected on the (001) and $(10\bar{1}0)$ surface BZs, respectively. As two CTWFs with $C = -3$ and three WPs with $C = +1$ are projected at the $\bar{\Gamma}$ and \bar{K} points of the (001) surface BZ, there are two types of topological nontrivial Fermi arcs, i.e., the sextuple-helicoid surface arcs around the $\bar{\Gamma}$ point and the triple-helicoid surface arcs around the \bar{K} point, as illustrated in Fig. 5(b). To visualize the helicoidal surface states, we calculate the surface LDOSs along two clockwise loops (loop₁ and loop₂) centered at $\bar{\Gamma}$ and \bar{K} [Figs. 5(c) and 5(d)]. For the loop₁, the six left-moving chiral edge modes appear inside the band gap, since loop₂ encompasses the three right-moving chiral edge modes. This hints they have opposite chirality. However, it only occurs in the triple-helicoid surface arcs on the $(10\bar{1}0)$ surface BZ, as shown in Fig. 5(f). The calculated surface LDOSs along anticlockwise loop₃ and clockwise loop₄ show that the three left-moving and right-moving chiral edge modes appear inside the band gap [Figs. 5(g) and 5(h)]. The Li_2CO_4 hosts the ultralong Fermi arcs, which makes it easier to be detected by experiments.

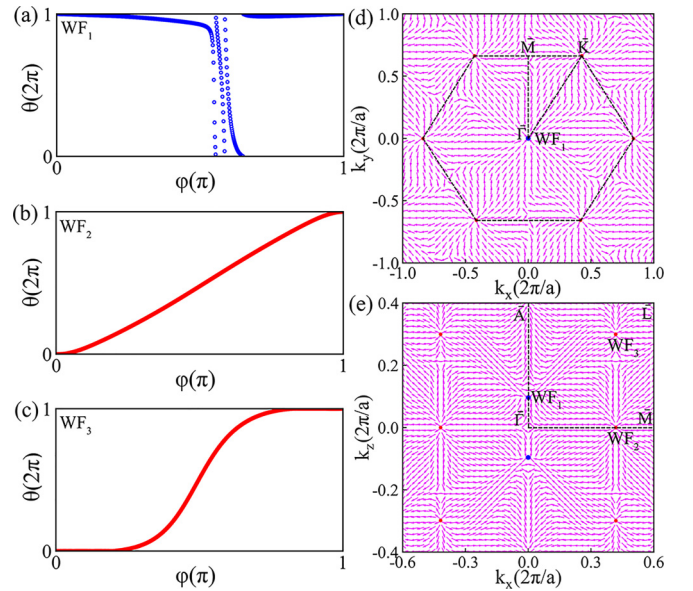


FIG. 4. (a)–(c) The evolutions of WCCs for WF_1 , WF_2 , and WF_3 . Here, $\varphi \in [0, \pi]$ is the polar angle, and $\theta \in [0, 2\pi]$ represents the evolution of the WCCs. The WPs are characterized by topological charges of -3 , $+1$, and $+1$, respectively. (d) and (e) The Berry curvature distributions of the (001) and $(10\bar{1}0)$ surface BZs. The WF_2 and WF_3 with $C = +1$ as the ‘‘source’’ flow into the ‘‘sink’’ generated by WF_1 with $C = -3$.

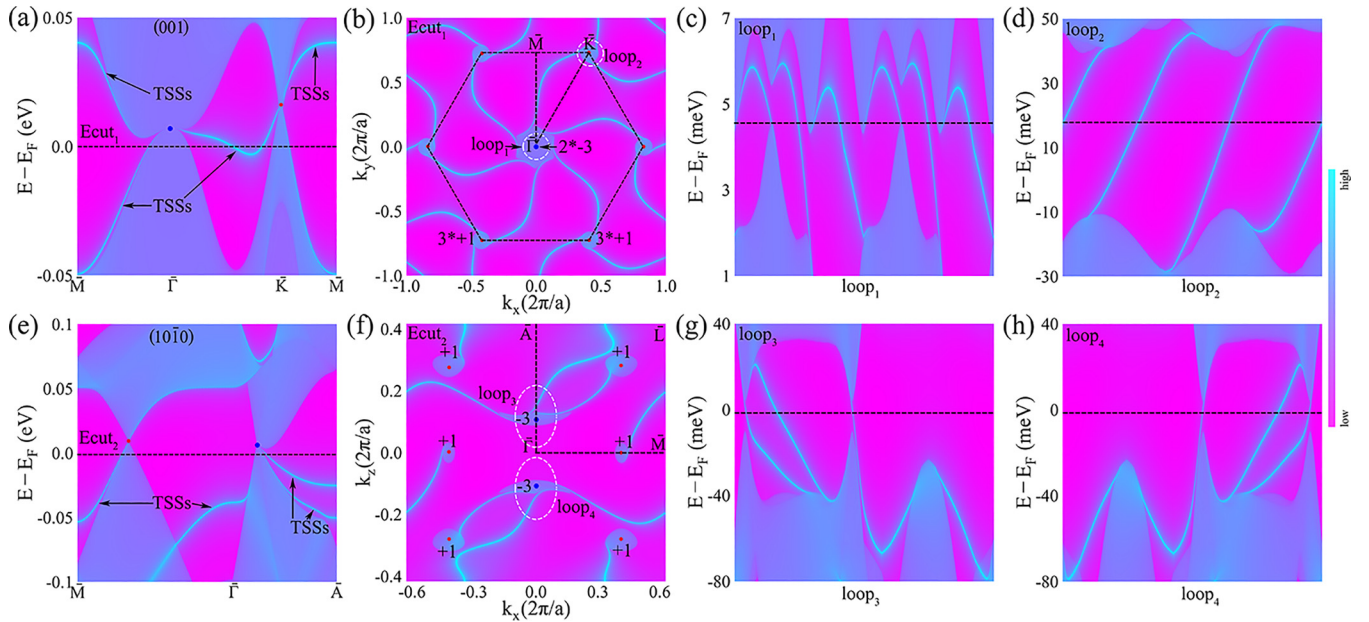


FIG. 5. (a) The LDOS along $\bar{M}-\bar{\Gamma}-\bar{K}-\bar{M}$ on the (001) surface BZ, where TSSs denote topological surface states. The black dashed line represents the isoenergy contours at the energy cut₁ ($E_{cut_1} = 0$ meV). (b) The corresponding Fermi arcs at $E_{cut_1} = 0$ meV and the positions of the WPs with the associated topological charges. (c) and (d) The surface LDOSs along two white clockwise loops (loop₁ and loop₂) centered at $\bar{\Gamma}$ and \bar{K} in (b). The black dashed lines are the reference line. It occurs in sextuple- and triple-helicoid TSSs, respectively. (e) The LDOS along $\bar{M}-\bar{\Gamma}-\bar{A}$ on the (10 $\bar{1}0$) surface BZ. The black dashed line represents the isoenergy contours at the energy cut₂ ($E_{cut_2} = -3$ meV). (f) The corresponding Fermi arcs at $E_{cut_2} = -3$ meV and the positions of the WPs with the associated topological charges. (g) and (h) The surface LDOSs along the white anticlockwise loop (loop₃) and clockwise loop (loop₄) centered at WF₁ in (f). It only occurs in triple-helicoid TSSs.

V. SUMMARY

In summary, based on symmetry arguments and the low-energy effective model, we identify that two chiral SGs (No. 173 and No. 182) can hold ideal hourglass-type CTWFs along the Γ -A path. Then, we take an ideal candidate Li_2CO_4 as an example, which possesses two CTWFs and six WPs, leading to sextuple- and triple-helicoid surface arcs on the (001) and (10 $\bar{1}0$) surface BZs, respectively. In addition, unlike spinful systems, in which the TSSs depend on the strength of SOC, the sextuple- and triple-helicoid surface arcs in spinless systems are distinct and well-separated, making them easier to be detected by experiments. Our work not only offers a method to search for twofold unconventional hourglass-type quasiparticles with nonlinear dispersion in 230 SGs but also

provides a platform to explore novel properties of unconventional quasiparticles in realistic materials. Furthermore, the large topological charge of CTWFs can lead to intriguing responses, such as significant quantized CPGE, which makes it a promising avenue for potential applications.

ACKNOWLEDGMENTS

This work was supported by the National Natural Science Foundation of China (NSFC, Grants No. 12174040, No. 12204074, No. 12222402, and No. 12347101), the China National Postdoctoral Program for Innovative Talent (Grant No. BX20220367), and Chongqing Natural Science Foundation (Grant No. cstc2020jcyj-msxmX0118).

- [1] Z. Wang, A. Alexandradinata, R. J. Cava, and B. A. Bernevig, Hourglass fermions, *Nature (London)* **532**, 189 (2016).
- [2] Y. Chen, H.-S. Kim, and H.-Y. Kee, Topological crystalline semimetals in nonsymmorphic lattices, *Phys. Rev. B* **93**, 155140 (2016).
- [3] L. Wang, S.-K. Jian, and H. Yao, Hourglass semimetals with nonsymmorphic symmetries in three dimensions, *Phys. Rev. B* **96**, 075110 (2017).
- [4] J. Ma, C. Yi, B. Lv, Z. Wang, S. Nie, L. Wang, L. Kong, Y. Huang, P. Richard, P. Zhang, K. Yaji, K. Kuroda, S. Shin, H. Weng, B. A. Bernevig, Y. Shi, T. Qian, and H. Ding, Experimental evidence of hourglass fermion in the candidate

nonsymmorphic topological insulator KHgSb , *Sci. Adv.* **3**, e1602415 (2017).

- [5] A. J. Liang, J. Jiang, M. X. Wang, Y. Sun, N. Kumar, C. Shekhar, C. Chen, H. Peng, C. W. Wang, X. Xu, H. F. Yang, S. T. Cui, G. H. Hong, Y.-Y. Xia, S.-K. Mo, Q. Gao, X. J. Zhou, L. X. Yang, C. Felser, B. H. Yan *et al.*, Observation of the topological surface state in the nonsymmorphic topological insulator KHgSb , *Phys. Rev. B* **96**, 165143 (2017).
- [6] L. Wu, F. Tang, and X. Wan, Exhaustive list of topological hourglass band crossings in 230 space groups, *Phys. Rev. B* **102**, 035106 (2020).

- [7] Y. Hu, X. Wan, and F. Tang, Magnetic hourglass fermions: From exhaustive symmetry conditions to high-throughput materials predictions, *Phys. Rev. B* **106**, 165128 (2022).
- [8] S.-S. Wang, Y. Liu, Z.-M. Yu, X.-L. Sheng, and S. A. Yang, Hourglass Dirac chain metal in rhenium dioxide, *Nat. Commun.* **8**, 1844 (2017).
- [9] B. Singh, B. Ghosh, C. Su, H. Lin, A. Agarwal, and A. Bansil, Topological hourglass Dirac semimetal in the nonpolar phase of Ag_2BiO_3 , *Phys. Rev. Lett.* **121**, 226401 (2018).
- [10] B. Fu, X. Fan, D. Ma, C.-C. Liu, and Y. Yao, Hourglasslike nodal net semimetal in Ag_2BiO_3 , *Phys. Rev. B* **98**, 075146 (2018).
- [11] D. Shao, H. Wang, T. Chen, P. Lu, Q. Gu, L. Sheng, D. Xing, and J. Sun, Composite topological nodal lines penetrating the Brillouin zone in orthorhombic AgF_2 , *npj Comput. Mater.* **5**, 5 (2019).
- [12] H. Zhang, X. Zhang, T. He, X. Dai, Y. Liu, G. Liu, L. Wang, and Y. Zhang, Three-dimensional Weyl hourglass networks in the nonsymmorphic half-metal Mg_2VO_4 , *Phys. Rev. B* **102**, 155116 (2020).
- [13] Z. F. Wang, B. Liu, and W. Zhu, Hourglass fermion in two-dimensional material, *Phys. Rev. Lett.* **123**, 126403 (2019).
- [14] W. Wu, Y. Jiao, S. Li, X.-L. Sheng, Z.-M. Yu, and S. A. Yang, Hourglass Weyl loops in two dimensions: Theory and material realization in monolayer GaTeI family, *Phys. Rev. Mater.* **3**, 054203 (2019).
- [15] R. Takahashi, M. Hirayama, and S. Murakami, Spinless hourglass nodal-line semimetals, *Phys. Rev. B* **96**, 155206 (2017).
- [16] S. M. Young and C. L. Kane, Dirac semimetals in two dimensions, *Phys. Rev. Lett.* **115**, 126803 (2015).
- [17] S. Li, Y. Liu, S.-S. Wang, Z.-M. Yu, S. Guan, X.-L. Sheng, Y. Yao, and S. A. Yang, Nonsymmorphic-symmetry-protected hourglass Dirac loop, nodal line, and Dirac point in bulk and monolayer X_3SiTe_6 ($X = \text{Ta}, \text{Nb}$), *Phys. Rev. B* **97**, 045131 (2018).
- [18] T. Bzdušek, Q. Wu, A. Rüegg, M. Sigrist, and A. A. Soluyanov, Nodal-chain metals, *Nature (London)* **538**, 75 (2016).
- [19] Z.-M. Yu, Z. Zhang, G.-B. Liu, W. Wu, X.-P. Li, R.-W. Zhang, S. A. Yang, and Y. Yao, Encyclopedia of emergent particles in three-dimensional crystals, *Sci. Bull.* **67**, 375 (2022).
- [20] S.-Y. Xu, I. Belopolski, N. Alidoust, M. Neupane, G. Bian, C. Zhang, R. Sankar, G. Chang, Z. Yuan, C.-C. Lee, S.-M. Huang, H. Zheng, J. Ma, D. S. Sanchez, B. Wang, A. Bansil, F. Chou, P. P. Shibayev, H. Lin, S. Jia *et al.*, Discovery of a Weyl fermion semimetal and topological Fermi arcs, *Science* **349**, 613 (2015).
- [21] B. Q. Lv, H. M. Weng, B. B. Fu, X. P. Wang, H. Miao, J. Ma, P. Richard, X. C. Huang, L. X. Zhao, G. F. Chen, Z. Fang, X. Dai, T. Qian, and H. Ding, Experimental discovery of Weyl semimetal TaAs, *Phys. Rev. X* **5**, 031013 (2015).
- [22] L. Lu, Z. Wang, D. Ye, L. Ran, L. Fu, J. D. Joannopoulos, and M. Soljacic, Experimental observation of Weyl points, *Science* **349**, 622 (2015).
- [23] P. Tang, Q. Zhou, and S.-C. Zhang, Multiple types of topological fermions in transition metal silicides, *Phys. Rev. Lett.* **119**, 206402 (2017).
- [24] G. Chang, S.-Y. Xu, B. J. Wieder, D. S. Sanchez, S.-M. Huang, I. Belopolski, T.-R. Chang, S. Zhang, A. Bansil, H. Lin, and M. Z. Hasan, Unconventional chiral fermions and large topological Fermi arcs in RhSi, *Phys. Rev. Lett.* **119**, 206401 (2017).
- [25] D. Takane, Z. Wang, S. Souma, K. Nakayama, T. Nakamura, H. Oinuma, Y. Nakata, H. Iwasawa, C. Cacho, T. Kim, K. Horiba, H. Kumigashira, T. Takahashi, Y. Ando, and T. Sato, Observation of chiral fermions with a large topological charge and associated Fermi-arc surface states in CoSi, *Phys. Rev. Lett.* **122**, 076402 (2019).
- [26] Z. Rao, H. Li, T. Zhang, S. Tian, C. Li, B. Fu, C. Tang, L. Wang, Z. Li, W. Fan, J. Li, Y. Huang, Z. Liu, Y. Long, C. Fang, H. Weng, Y. Shi, H. Lei, Y. Sun, T. Qian *et al.*, Observation of unconventional chiral fermions with long Fermi arcs in CoSi, *Nature (London)* **567**, 496 (2019).
- [27] E. J. König, H.-Y. Xie, D. A. Pesin, and A. Levchenko, Photogalvanic effect in Weyl semimetals, *Phys. Rev. B* **96**, 075123 (2017).
- [28] F. de Juan, A. G. Grushin, T. Morimoto, and J. E. Moore, Photogalvanic effect in Weyl semimetals, *Nat. Commun.* **8**, 15995 (2017).
- [29] F. Flicker, F. de Juan, B. Bradlyn, T. Morimoto, M. G. Vergniory, and A. G. Grushin, Chiral optical response of multi-fold fermions, *Phys. Rev. B* **98**, 155145 (2018).
- [30] E.-G. Moon, C. Xu, Y. B. Kim, and L. Balents, Non-Fermi-liquid and topological states with strong spin-orbit coupling, *Phys. Rev. Lett.* **111**, 206401 (2013).
- [31] I. F. Herbut and L. Janssen, Topological Mott insulator in three-dimensional systems with quadratic band touching, *Phys. Rev. Lett.* **113**, 106401 (2014).
- [32] S.-K. Jian and H. Yao, Correlated double-Weyl semimetals with Coulomb interactions: Possible applications to HgCr_2Se_4 and SrSi_2 , *Phys. Rev. B* **92**, 045121 (2015).
- [33] S.-K. Jian and H. Yao, Fermion-induced quantum critical points in three-dimensional Weyl semimetals, *Phys. Rev. B* **96**, 155112 (2017).
- [34] X. Wang, F. Zhou, Z. Zhang, Z.-M. Yu, and Y. Yao, Hourglass charge-three Weyl phonons, *Phys. Rev. B* **106**, 214309 (2022).
- [35] G. Liu, Z. Chen, P. Wu, and H. Xu, Triple hourglass Weyl phonons, *Phys. Rev. B* **106**, 214308 (2022).
- [36] P. Huang, X. Chen, P. Zhang, H. Sun, S. Xu, W. Xiong, R. Wang, H. Zhang, Q. Liu, and X. Zhang, Crystalline chirality and interlocked double hourglass Weyl fermion in polyhedral-intercalated transition metal dichalcogenides, *NPG Asia Mater.* **13**, 49 (2021).
- [37] J. Wang, H. Yuan, W. Wang, G. Ding, X.-P. Li, and X. Wang, Fully spin-polarized hourglass charge-three Weyl points and sextuple-helicoid surface arcs in $P6_322$ -type BaNiO_6 , *Phys. Rev. B* **108**, 054424 (2023).
- [38] Y. Li, L. Wu, S. Zhou, and H. Wu, $P6_322$ -type SrNiO_6 : An ideal half-metallic candidate with a fully spin-polarized Weyl complex, *Results Phys.* **52**, 106829 (2023).
- [39] Y. Yao, F. Ye, X.-L. Qi, S.-C. Zhang, and Z. Fang, Spin-orbit gap of graphene: First-principles calculations, *Phys. Rev. B* **75**, 041401(R) (2007).
- [40] C. Zhang, X.-Y. Ding, L.-Y. Gan, Y. Cao, B.-S. Li, X. Wu, and R. Wang, Symmetry-guaranteed ideal Weyl semimetallic phase in face-centered orthogonal C_6 , *Phys. Rev. B* **101**, 235119 (2020).
- [41] J. Wei, W. Kong, X. Xiao, R. Wang, L.-Y. Gan, J. Fan, and X. Wu, Dirac fermions in the boron nitride monolayer with a tetragon, *J. Phys. Chem. Lett.* **13**, 5508 (2022).
- [42] W. Kong, R. Wang, X. Xiao, F. Zhan, L.-Y. Gan, J. Wei, J. Fan, and X. Wu, Dirac fermions in graphene with stacking fault

- induced periodic line defects, *J. Phys. Chem. Lett.* **12**, 10874 (2021).
- [43] W. Wu, Y. Xie, and Y. Chen, Nodal points in three-dimensional carbon networks without inversion symmetry, *Phys. Rev. Mater.* **5**, 104201 (2021).
- [44] T. Deng, B. Zheng, F. Zhan, J. Fan, X. Wu, and R. Wang, Photoinduced Floquet mixed-Weyl semimetallic phase in a carbon allotrope, *Phys. Rev. B* **102**, 201105(R) (2020).
- [45] H. Weng, Y. Liang, Q. Xu, R. Yu, Z. Fang, X. Dai, and Y. Kawazoe, Topological node-line semimetal in three-dimensional graphene networks, *Phys. Rev. B* **92**, 045108 (2015).
- [46] J.-T. Wang, H. Weng, S. Nie, Z. Fang, Y. Kawazoe, and C. Chen, Body-centered orthorhombic C_{16} : A novel topological node-line semimetal, *Phys. Rev. Lett.* **116**, 195501 (2016).
- [47] Y. Cheng, X. Feng, X. Cao, B. Wen, Q. Wang, Y. Kawazoe, and P. Jena, Body-centered tetragonal C_{16} : A novel topological node-line semimetallic carbon composed of tetrarings, *Small* **13**, 1602894 (2017).
- [48] K. Bu, Y. Qian, J.-T. Wang, and H. Weng, Hybrid nodal chain in an orthorhombic graphene network, *Phys. Rev. B* **103**, L081108 (2021).
- [49] J.-T. Wang, S. Nie, H. Weng, Y. Kawazoe, and C. Chen, Topological nodal-net semimetal in a graphene network structure, *Phys. Rev. Lett.* **120**, 026402 (2018).
- [50] Y. Chen, Y. Xie, S. A. Yang, H. Pan, F. Zhang, M. L. Cohen, and S. Zhang, Nanostructured carbon allotropes with Weyl-like loops and points, *Nano Lett.* **15**, 6974 (2015).
- [51] C. Zhong, Y. Chen, Y. Xie, S. A. Yang, M. L. Cohen, and S. B. Zhang, Towards three-dimensional Weyl-surface semimetals in graphene networks, *Nanoscale* **8**, 7232 (2016).
- [52] Y. Qie, J. Liu, S. Wang, Q. Sun, and P. Jena, Tetragonal C_{24} : a topological nodal-surface semimetal with potential as an anode material for sodium ion batteries, *J. Mater. Chem. A* **7**, 5733 (2019).
- [53] J. Zhang, R. Wang, X. Zhu, A. Pan, C. Han, X. Li, D. Zhao, C. Ma, W. Wang, H. Su, and C. Niu, Pseudo-topotactic conversion of carbon nanotubes to T-carbon nanowires under picosecond laser irradiation in methanol, *Nat. Commun.* **8**, 683 (2017).
- [54] X.-W. Yi, Z. Zhang, Z.-W. Liao, X.-J. Dong, J.-Y. You, and G. Su, T-carbon: Experiments, properties, potential applications and derivatives, *Nano Today* **42**, 101346 (2022).
- [55] J. D. Koralek, C. P. Weber, J. Orenstein, B. A. Bernevig, S.-C. Zhang, S. Mack, and D. D. Awschalom, Emergence of the persistent spin helix in semiconductor quantum wells, *Nature (London)* **458**, 610 (2009).
- [56] P. Hohenberg and W. Kohn, Inhomogeneous electron gas, *Phys. Rev.* **136**, B864 (1964).
- [57] W. Kohn and L. Sham, Self-consistent equations including exchange and correlation effects, *Phys. Rev.* **140**, A1133 (1965).
- [58] G. Kresse and J. Furthmüller, Efficiency of ab-initio total energy calculations for metals and semiconductors using a plane-wave basis set, *Comput. Mater. Sci.* **6**, 15 (1996).
- [59] G. Kresse and J. Furthmüller, Efficient iterative schemes for ab initio total-energy calculations using a plane-wave basis set, *Phys. Rev. B* **54**, 11169 (1996).
- [60] J. P. Perdew, K. Burke, and M. Ernzerhof, Generalized gradient approximation made simple, *Phys. Rev. Lett.* **77**, 3865 (1996).
- [61] P. E. Blöchl, Projector augmented-wave method, *Phys. Rev. B* **50**, 17953 (1994).
- [62] H. J. Monkhorst and J. D. Pack, Special points for Brillouin-zone integrations, *Phys. Rev. B* **13**, 5188 (1976).
- [63] A. Togo, F. Oba, and I. Tanaka, First-principles calculations of the ferroelastic transition between rutile-type and $CaCl_2$ -type SiO_2 at high pressures, *Phys. Rev. B* **78**, 134106 (2008).
- [64] X. Gonze and C. Lee, Dynamical matrices, born effective charges, dielectric permittivity tensors, and interatomic force constants from density-functional perturbation theory, *Phys. Rev. B* **55**, 10355 (1997).
- [65] C. Fang, M. J. Gilbert, X. Dai, and B. A. Bernevig, Multi-Weyl topological semimetals stabilized by point group symmetry, *Phys. Rev. Lett.* **108**, 266802 (2012).
- [66] S. S. Tsirkin, I. Souza, and D. Vanderbilt, Composite Weyl nodes stabilized by screw symmetry with and without time-reversal invariance, *Phys. Rev. B* **96**, 045102 (2017).
- [67] Y. J. Jin, Y. Xu, Z. J. Chen, and H. Xu, Type-II quadratic and cubic Weyl fermions, *Phys. Rev. B* **105**, 035141 (2022).
- [68] B. Zheng, F. Zhan, X. Wu, R. Wang, and J. Fan, Hourglass phonons jointly protected by symmorphic and nonsymmorphic symmetries, *Phys. Rev. B* **104**, L060301 (2021).
- [69] Z. J. Chen, Z. J. Xie, Y. J. Jin, G. Liu, and H. Xu, Hybrid nodal-ring phonons with hourglass dispersion in $AgAlO_2$, *Phys. Rev. Mater.* **6**, 034202 (2022).
- [70] See Supplemental Material at <http://link.aps.org/supplemental/10.1103/PhysRevB.109.075160> for band dispersions along the different planes and the topological charges of each bands based on the Hamiltonian, character table of PG C_6 , phonon dispersions, bulk band structures with/without SOC, and the LDOSs and Fermi arcs of crystal structure on the (001) and (10 $\bar{1}$ 0) surfaces BZ of the candidate materials (Li_2CO_4 , $LiBeBO_4$, $NaBeBO_4$, $MgSi_2N_4$, and $AlSi_2$), which includes Refs. [82,83].
- [71] S. E. Han, C. Lee, E.-G. Moon, and H. Min, Emergent anisotropic non-Fermi liquid at a topological phase transition in three dimensions, *Phys. Rev. Lett.* **122**, 187601 (2019).
- [72] J.-R. Wang, G.-Z. Liu, and C.-J. Zhang, Topological quantum critical point in a triple-Weyl semimetal: Non-Fermi-liquid behavior and instabilities, *Phys. Rev. B* **99**, 195119 (2019).
- [73] R. Yu, X. L. Qi, A. Bernevig, Z. Fang, and X. Dai, Equivalent expression of \mathbb{Z}_2 topological invariant for band insulators using the non-Abelian Berry connection, *Phys. Rev. B* **84**, 075119 (2011).
- [74] C. Bradley and A. Cracknell, *The Mathematical Theory of Symmetry in Solids: Representation Theory for Point Groups and Space Groups* (Oxford University Press, Oxford, 2009).
- [75] N. Marzari and D. Vanderbilt, Maximally localized generalized Wannier functions for composite energy bands, *Phys. Rev. B* **56**, 12847 (1997).
- [76] A. A. Mostofi, J. R. Yates, Y.-S. Lee, I. Souza, D. Vanderbilt, and N. Marzari, WANNIER90: A tool for obtaining maximally-localised Wannier functions, *Comput. Phys. Commun.* **178**, 685 (2008).
- [77] H. Nielsen and M. Ninomiya, Absence of neutrinos on a lattice: (I). Proof by homotopy theory, *Nucl. Phys. B* **185**, 20 (1981).
- [78] H. Nielsen and M. Ninomiya, Absence of neutrinos on a lattice: (II). Intuitive topological proof, *Nucl. Phys. B* **193**, 173 (1981).
- [79] M. P. L. Sancho, J. M. L. Sancho, and J. Rubio, Quick iterative scheme for the calculation of transfer

- matrices: application to Mo (100), *J. Phys. F* **14**, 1205 (1984).
- [80] M. P. L. Sancho, J. M. L. Sancho, J. M. L. Sancho, and J. Rubio, Highly convergent schemes for the calculation of bulk and surface Green functions, *J. Phys. F* **15**, 851 (1985).
- [81] Q. Wu, S. Zhang, H.-F. Song, M. Troyer, and A. A. Soluyanov, Wannertools: An open-source software package for novel topological materials, *Comput. Phys. Commun.* **224**, 405 (2018).
- [82] M. Born, K. Huang, and M. Lax, Dynamical theory of crystal lattices, *Am. J. Phys.* **23**, 474 (1955).
- [83] F. Mouhat and F. X. Coudert, Necessary and sufficient elastic stability conditions in various crystal systems, *Phys. Rev. B* **90**, 224104 (2014).